



MIT Open Access Articles

Simulations of Collision Cascades in Cu–Nb Layered Composites Using an EAM Interatomic Potential

The MIT Faculty has made this article openly available. **Please share** how this access benefits you. Your story matters.

Citation	DEMKOWICZ, M. J., and R. G. HOAGLAND. "SIMULATIONS OF COLLISION CASCADES IN Cu–Nb LAYERED COMPOSITES USING AN EAM INTERATOMIC POTENTIAL." International Journal of Applied Mechanics 01, no. 03 (September 2009): 421-442.
As Published	http://dx.doi.org/10.1142/S1758825109000216
Version	Author's final manuscript
Citable link	http://hdl.handle.net/1721.1/80853
Terms of Use	Creative Commons Attribution-Noncommercial-Share Alike 3.0
Detailed Terms	http://creativecommons.org/licenses/by-nc-sa/3.0/

Simulations of collision cascades in Cu-Nb layered composites using an EAM interatomic potential

M. J. Demkowicz^{1, 2, *}, R. G. Hoagland¹

¹MST-8: Structure-Property Relations Group, Los Alamos National Laboratory, Los Alamos, NM 87545

²Department of Materials Science and Engineering, Massachusetts Institute of Technology, Cambridge, MA 02139

Keywords: composites, radiation, molecular dynamics

The embedded atom method (EAM) is used to construct an interatomic potential for modeling interfaces in Cu-Nb nanocomposites. Implementation of the Ziegler-Biersack-Littmark (ZBL) model for short-range interatomic interactions enables studies of response to ion bombardment. Collision cascades are modeled in fcc Cu, bcc Nb, and in Cu-Nb layered composites in the experimentally-observed Kurdjumov-Sachs (KS) orientation relation. The interfaces in these composites reduce the number of vacancies and interstitials created per keV of the primary knock-on atom (PKA) by 50-70% compared to fcc Cu or bcc Nb.

1. Background

Multilayer nanocomposites of immiscible elements such as Cu and Nb exhibit markedly different response to radiation than the component elements themselves, both with respect to accumulation of damage [1-4] and diffusion and precipitation of implanted species like He [5, 6]. Morphologically stable under elevated temperature annealing [7] and high dose ion implantation [1, 2, 6], these materials can nevertheless be amorphized given sufficient primary knock-on atom (PKA) energies and low enough temperatures [8, 9].

The microstructural features that most directly influence the response of multilayer nanocomposites to irradiation are the interfaces between successive layers [4]. In sputter-deposited Cu-Nb multilayer films, these interfaces are efficient sinks and recombination surfaces for radiation-induced vacancies and interstitials. They have also been found to govern the material's mechanical properties [10, 11]. Understanding the response of multilayer nanocomposites to radiation and

* Corresponding author: demkowicz@mit.edu

mechanical loading therefore requires detailed studies of interface behavior using methods like atomistic modeling. Because the necessary simulations typically require systems containing tens of thousands of atoms or more, they cannot currently be performed using quantum mechanical treatments of bonding. Instead, interatomic forces are modeled using effective interaction potentials like embedded atom (EAM) [12], modified embedded atom (MEAM) [13, 14], or bond order [15-17]. This paper describes an EAM effective interaction potential designed for collision cascade simulations in the Cu-Nb system.

2. Construction of potential

2.1 Form of two-element EAM potentials

We use the embedded-atom method (EAM) [12] to construct a Cu-Nb potential. This method has proven successful in modeling the properties of elemental fcc and bcc metals [18-21] as well as some of their alloys [22, 23]. The construction of EAM potentials for multi-element systems has been reviewed by Voter [24]. For systems with atoms at positions $\{\vec{r}_i\}$ such potentials have the form

$$V(\{\vec{r}_i\}) = \sum_{i < j} \phi_{e_i e_j}(r_{ij}) + \sum_i F_{e_i}(\bar{\rho}_i) \quad (1)$$

$$\bar{\rho}_i = \sum_j \rho_{e_j}(r_{ij})$$

Here $\phi_{e_i e_j}(r_{ij})$ is a direct two-body interaction between atoms i and j that depends only on the interatomic separation r_{ij} . The total effective electron density $\bar{\rho}_i$ at atomic site i contributes to the total system energy through the embedding function F_{e_i} . Function $\rho_{e_j}(r_{ij})$ represents the contribution to the total effective electron density $\bar{\rho}_i$ at atom i due to atom j a distance r_{ij} away. The electron densities $\bar{\rho}_i$ and $\rho_{e_j}(r_{ij})$ have received a variety of physical interpretations [24-26]. We adopt the outlook that these functions can be freely adjusted to construct potentials with the desired properties, albeit ones whose form and purpose have been motivated by physical insight into the nature of metallic bonding [26]. Subscripts e_i and e_j denote the element types of atoms i and j . Thus, the form of the embedding function F_{e_i} and electron density contribution ρ_{e_j} vary according to element type while the form of the two-body interaction $\phi_{e_i e_j}$ varies by pairs of element types.

An EAM potential for an A-B (two-element) system can be created starting from single-element potentials for elements A and B if the two-body interaction ϕ_{AB} is specified. Four additional fitting parameters g_A , g_B , s_A , and s_B arise from the transformations

$$\begin{aligned} F'_x(\bar{\rho}) &= F_x(\bar{\rho}) + g_x \bar{\rho} \\ \phi'_x(r) &= \phi_x(r) - 2g_x \rho_x(r) \end{aligned} \quad (2)$$

and

$$\begin{aligned} \rho'_x(r) &= s_x \rho_x(r) \\ F'_x(\bar{\rho}) &= F_x(\bar{\rho}/s_x). \end{aligned} \quad (3)$$

Potentials for the single element x are invariant with respect to the transformations in eqn.s 2 and 3 for any values of g_x and s_x , but multiple-element EAM potentials are not, giving rise to the four fitting parameters mentioned above. One of s_A or s_B may be fixed to a specific numerical value without loss of generality since only the ratio of these parameters influences the overall A-B potential. Finally, the transformations in eqn.s 2 and 3 must be applied in a consistent order, as a multi-element potential is not invariant with respect to their interchange. We choose to apply eqn. 2 first followed by eqn. 3.

Despite its simplicity, the EAM potential form described above is sufficient to model many binary systems. It is especially straightforward to apply to elements that do not form compounds, including systems with full solid solubility like Ag-Au or completely immiscible ones like Cu-Nb.

2.2 Fitting a Cu-Nb EAM potential

In this work we construct a Cu-Nb EAM potential using a Cu single-element potential due to Voter [18] and a Nb potential created using an approach similar to that of Johnson and Oh [21]. The construction of these single-element potentials is paraphrased in appendix A.

Direct two-body interactions between Cu and Nb atoms separated by a distance r are modeled using the Morse function

$$\phi_{CuNb}(r) = D_M \left(1 - e^{-\alpha_M(r-R_M)}\right)^2 - D_M \quad (4)$$

modified so that its value and that of its first derivative smoothly approach zero at a specified cutoff radius r_{cut} :

$$\phi'_{CuNb}(r) = \phi_{CuNb}(r) - \phi_{CuNb}(r_{cut}) + \frac{r_{cut}}{20} \left(1 - r^{20}/r_{cut}^{20}\right) \frac{d\phi_{CuNb}}{dr} \Big|_{r=r_{cut}} . \quad (5)$$

The quantities D_M , R_M , α_M , and r_{cut} in eqn.s 4 and 5 are used as fitting parameters that can be adjusted to optimize the performance of the two-element Cu-Nb EAM potential. The transformations in eqn.s 2 and 3 provide three additional fitting parameters g_{Cu} , g_{Nb} , s_{Nb} with $s_{Cu} \equiv 1$, without loss of generality.

The fitting parameters were chosen so that the resulting potential would reproduce several physical properties of the Cu-Nb system: the dilute enthalpies of mixing of Cu in Nb $\Delta E_{(Cu \text{ in Nb})}$ and of Nb in Cu $\Delta E_{(Nb \text{ in Cu})}$ as well as the lattice parameter a_0 and bulk modulus B of a hypothetical Cu-Nb compound in the CsCl structure. The values of the dilute enthalpies of mixing were taken from fits to the Cu-Nb phase diagram [27] while a_0 and B were obtained by first principles calculations using VASP [28, 29].

The two-element potential described by a set of fitting parameters g_{Cu} , g_{Nb} , s_{Nb} , D_M , R_M , α_M , r_{cut} can be used to compute the predicted physical properties $\Delta E'_{(Cu \text{ in Nb})}$, $\Delta E'_{(Nb \text{ in Cu})}$, a'_0 , and B' . Then starting from any given initial values, the fitting parameters can be refined by requiring them to minimize a cost function χ that quantifies the deviation of the predicted from the target physical properties:

$$\chi = b_1 \cdot \left(\Delta E'_{(Cu \text{ in Nb})} - \Delta E_{(Cu \text{ in Nb})}\right)^2 + b_2 \cdot \left(\Delta E'_{(Nb \text{ in Cu})} - \Delta E_{(Nb \text{ in Cu})}\right)^2 + \quad (6)$$

$$b_3 \cdot (a'_0 - a_0)^2 + b_4 \cdot (B' - B)^2 .$$

Here the b_i are arbitrary weighting factors that influence the accuracy to which the different physical properties are reproduced by minimizing χ . χ would achieve a value of zero if the EAM potential were to perfectly reproduce all the target values of the physical properties, though it is not guaranteed this would occur for any set of fitting parameters within the EAM formalism. Because χ is a complicated function

of the fitting parameters, it is impracticable to analytically express the derivatives of χ with respect to them. We therefore choose to find minima of χ using the simplex method [30, 31], which does not require the gradient of the function being minimized.

Minimization of χ beginning with different initial values of the fitting parameters results in good fits being achieved for unlike final values of the fitting parameters, demonstrating that χ is a function containing multiple minima. Tables I and II list the fitting parameters and physical properties for two different Cu-Nb EAM potentials, labeled “1” and “2.” Although the fitting parameters are very different for these two potentials, both reproduce the target values of the physical properties with comparable accuracy. To choose between these different parameterizations we additionally require that it be possible to smoothly join the Cu-Nb EAM potential to the ZBL universal repulsive potential (see Appendix B) without creating spurious energy minima at low interatomic separations, as described in the next subsection.

Table I: Fitting parameters for two different Cu-Nb EAM potentials, both of which predict physical properties with similar accuracy (see Table II).

Parameters	g_{Cu}	g_{Nb}	s_{Nb}	D_{M} (eV)	R_{M} (Å)	α_{M} (Å ⁻¹)	r_{cut} (Å)
EAM 1	30.0	-0.0891	0.00459	2.608	1.815	0.483	3.806
EAM 2	-3.71	-0.848	0.0170	0.572	2.509	2.327	4.402

Table II: Physical properties predicted by two Cu-Nb EAM potentials with different fitting parameters (see Table I).

	$\Delta E_{(\text{Cu in Nb})}$ (eV)	$\Delta E_{(\text{Nb in Cu})}$ (eV)	a_0 (Å)	B (GPa)
Experiment/VASP	1.02 [27]	0.48 [27]	3.22 (VASP)	168 (VASP)
EAM 1	1.03	0.38	3.19	188
EAM 2	1.03	0.50	3.23	176

In a previous publication [32] we described two different flaw-free atomic configurations that can form at a Cu-Nb interface in the Kurdjumov-Sachs orientation relation. After the positions of all their atoms are allowed to fully relax, both configurations exhibit nearly degenerate interface energies, independent of the parameterization of the of the EAM potential used in the relaxation simulations. The differences in interfaces energies between these two interfaces—in both their reference and relaxed states—determined using the two Cu-Nb EAM potentials described above are listed in table III. As expected, the energies of the relaxed interfaces are within about 3 mJ/m² for both potentials despite a difference of up to about 170 mJ/m² for the reference states. This indifference of relaxed interface

energies to the details of atomic interactions arises from the geometrical transformation relating the two configurations [32].

Table III: Differences in interface energies $\Delta\gamma_{KS_2-KS_1} = \gamma_{KS_2} - \gamma_{KS_1}$ (mJ/m²) between the two interface configurations (KS₁ and KS₂) described in Ref. 32, in both their reference and relaxed states.

State	unrelaxed	relaxed
EAM 1	-169	-0.83
EAM 2	-112	-3.05

2.3 Short-range repulsive forces

During high-energy ion bombardment, atoms in the target material may gain enough energy to approach neighboring atoms to distances much shorter than those seen in solids at thermal equilibrium. The strong mutual repulsion felt by atoms at such short separations can be modeled by the two-body ZBL potential (Appendix B). For a given pair of elements, this interaction is incorporated into the Cu-Nb potential by joining the ZBL function to a spline at interatomic distance r_a and then joining the spline to the corresponding EAM direct pair interaction term (ϕ_{CuCu} , ϕ_{NbNb} , or ϕ_{CuNb}) at an interatomic distance $r_b > r_a$. The spline has the form

$$\phi_s(r) = a_0 + a_1 r^{-1} + a_2 r^{-2} + a_3 r^{-3}. \quad (7)$$

The fitting constants a_i are chosen so that the spline matches the value of EAM two-body term under consideration $\phi_{EAM}(r_b)$ and that of its first derivative $\phi'_{EAM}(r_b)$ at r_b as well as the value of the ZBL potential $\phi_{ZBL}(r_a)$ and that of its first derivative $\phi'_{ZBL}(r_a)$ at $r_a < r_b$. This is accomplished by solving the linear system

$$\begin{bmatrix} 1 & r_a^{-1} & r_a^{-2} & r_a^{-3} \\ 1 & r_b^{-1} & r_b^{-2} & r_b^{-3} \\ 0 & -r_a^{-2} & -2r_a^{-3} & -3r_a^{-4} \\ 0 & -r_b^{-2} & -2r_b^{-3} & -3r_b^{-4} \end{bmatrix} \cdot \begin{bmatrix} a_0 \\ a_1 \\ a_2 \\ a_3 \end{bmatrix} = \begin{bmatrix} \phi_{ZBL}(r_a) \\ \phi_{EAM}(r_b) \\ \phi'_{ZBL}(r_a) \\ \phi'_{EAM}(r_b) \end{bmatrix}. \quad (8)$$

In some EAM parameterizations (e.g. in the Nb potential described in Appendix A) the direct two-body contributions to the electron density may diverge at short interatomic separations. Thus, to prevent unintended influence of the embedding energy on two-body repulsion at short separations, the two-body contributions to electron density $\rho_{Cu}(r)$ and $\rho_{Nb}(r)$ are forced to approach zero smoothly at $r = 0$. This is accomplished by fitting a spline

$$\rho_s(r) = a_0 + a_1 r + a_2 r^2 + a_3 r^3 \quad (9)$$

to any given $\rho_{EAM}(r)$ so that it matches the value of the electron density contribution $\rho_{EAM}(r_b)$ and that of its first derivative $\rho'_{EAM}(r_b)$ at r_b . The requirement $\rho_s(0) = \rho'_s(0) = 0$ forces $a_0 = a_1 = 0$. The remaining constants a_2 and a_3 are found by solving the linear system

$$\begin{bmatrix} r_b^2 & r_b^3 \\ 2r_b & 3r_b^2 \end{bmatrix} \cdot \begin{bmatrix} a_2 \\ a_3 \end{bmatrix} = \begin{bmatrix} \rho_{EAM}(r_b) \\ \rho'_{EAM}(r_b) \end{bmatrix}. \quad (10)$$

For any given single element, the same value of r_b is used in eqn.s 8 and 10.

The procedure for fitting a Cu-Nb EAM potential described in subsection 2.2 tries to reproduce the values of quantities such as enthalpies of mixing, lattice parameters, and elastic constants, none of which probe the forces present at small atomic separations. Extending the potential to short interatomic distances by joining with ZBL may therefore result in unexpected and sometimes unphysical behaviors. For example, when joined with ZBL, Cu-Nb potential “EAM 2” from table I predicts a very deep, spurious cohesive energy minimum at low lattice parameters for Cu-Nb in the CsCl structure. On the other hand, Cu-Nb potential “EAM 1” from table I does not. Figure 1 compares the cohesive energy per atom vs. lattice parameter curves for these two parameterizations.

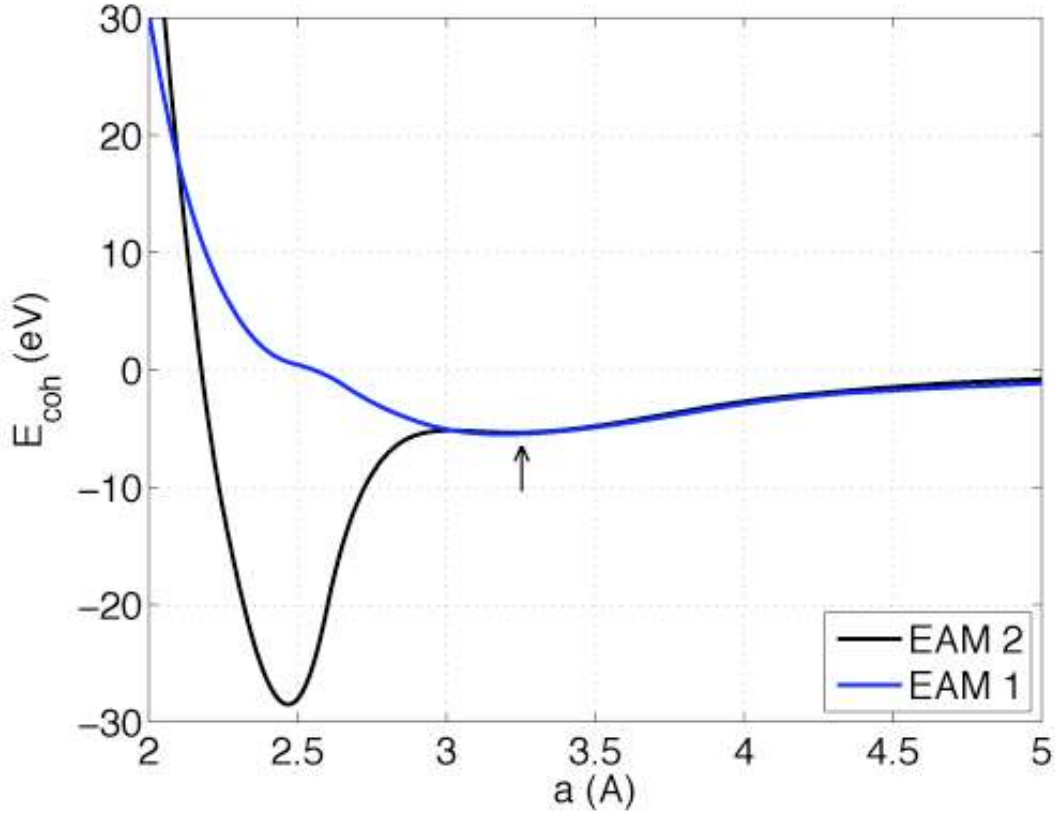


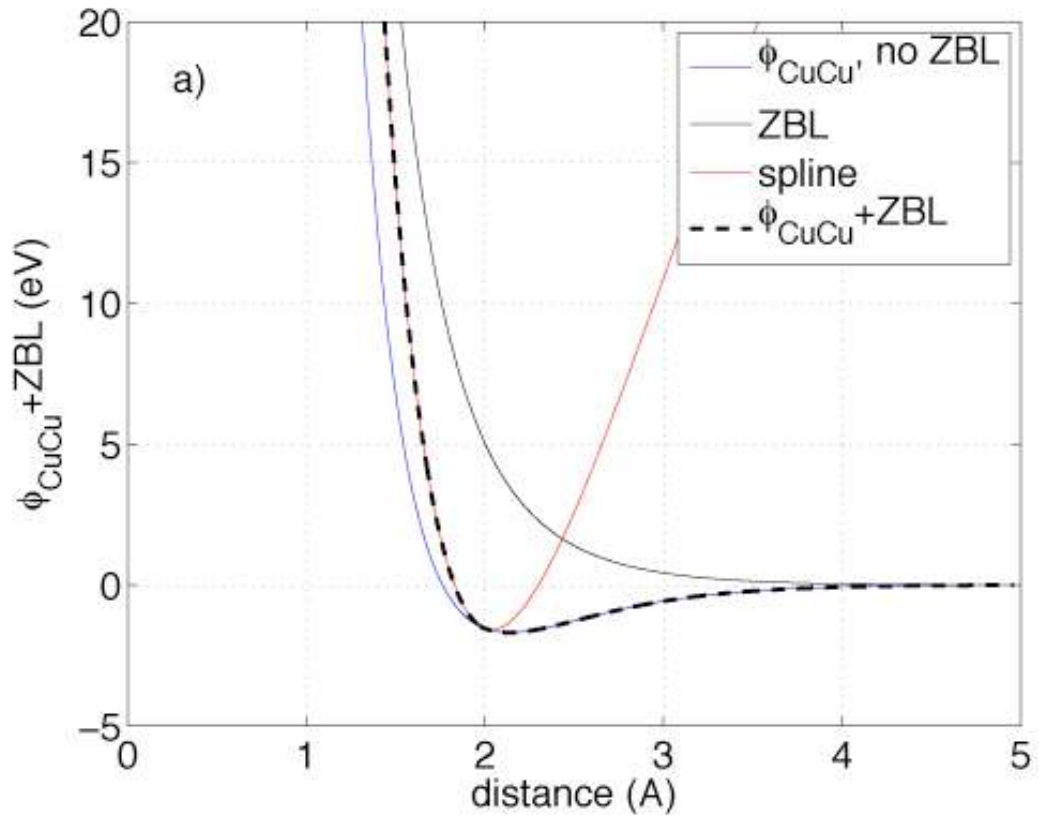
Figure 1: Cohesive energy per atom E_{coh} (eV) vs. lattice parameter a (Å) for Cu-Nb in the CsCl structure as predicted by the two EAM potentials in table I. “EAM 2” has a deep, spurious minimum at lattice parameter just below 2.5Å while “EAM 1” does not. The fitted values of lattice parameter and bulk modulus for Cu-Nb in the CsCl structure arise from the minimum indicated by the arrow.

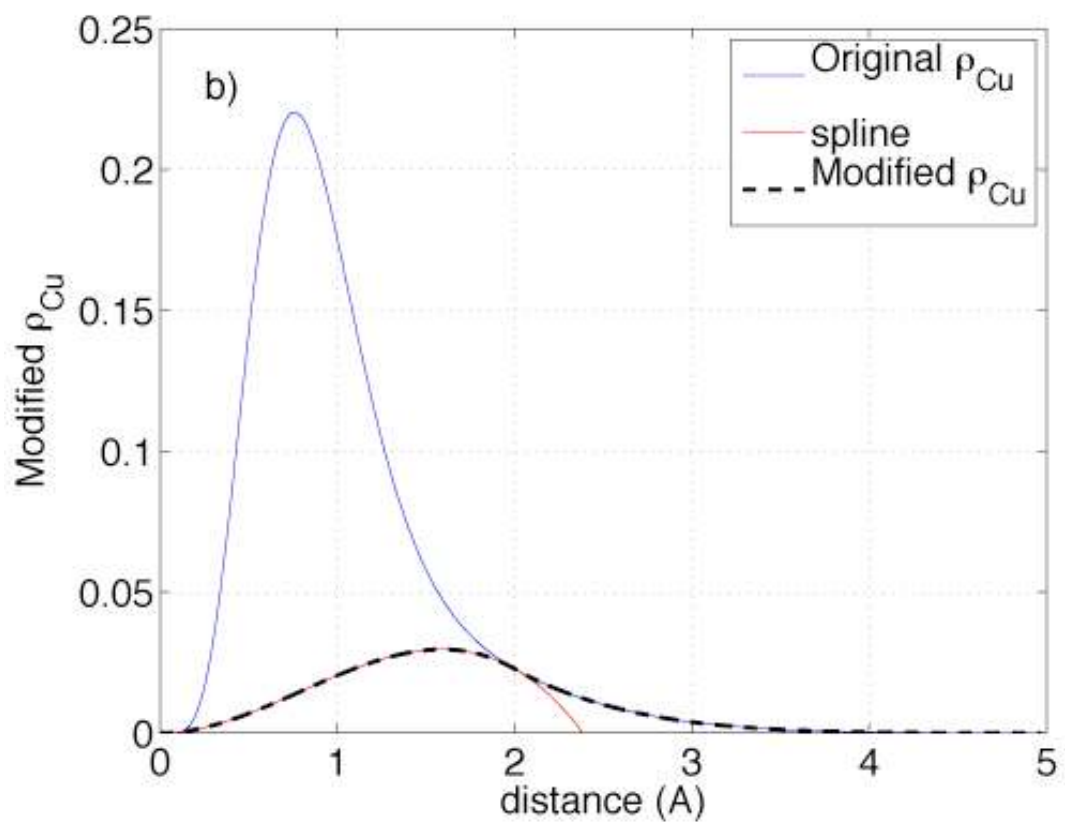
Further investigation of Cu-Nb potential “EAM 1” (cohesive energies for other crystal structures, dimer energies, and the collision cascades described in section 3) never revealed any spurious energy minima. “EAM 1” from table I was therefore selected in preference of “EAM 2” and will be used for the remainder of the work described here. Table IV lists the spline fitting parameters r_a and r_b for this parameterization while figure 2 presents plots of the various functions that define this EAM potential.

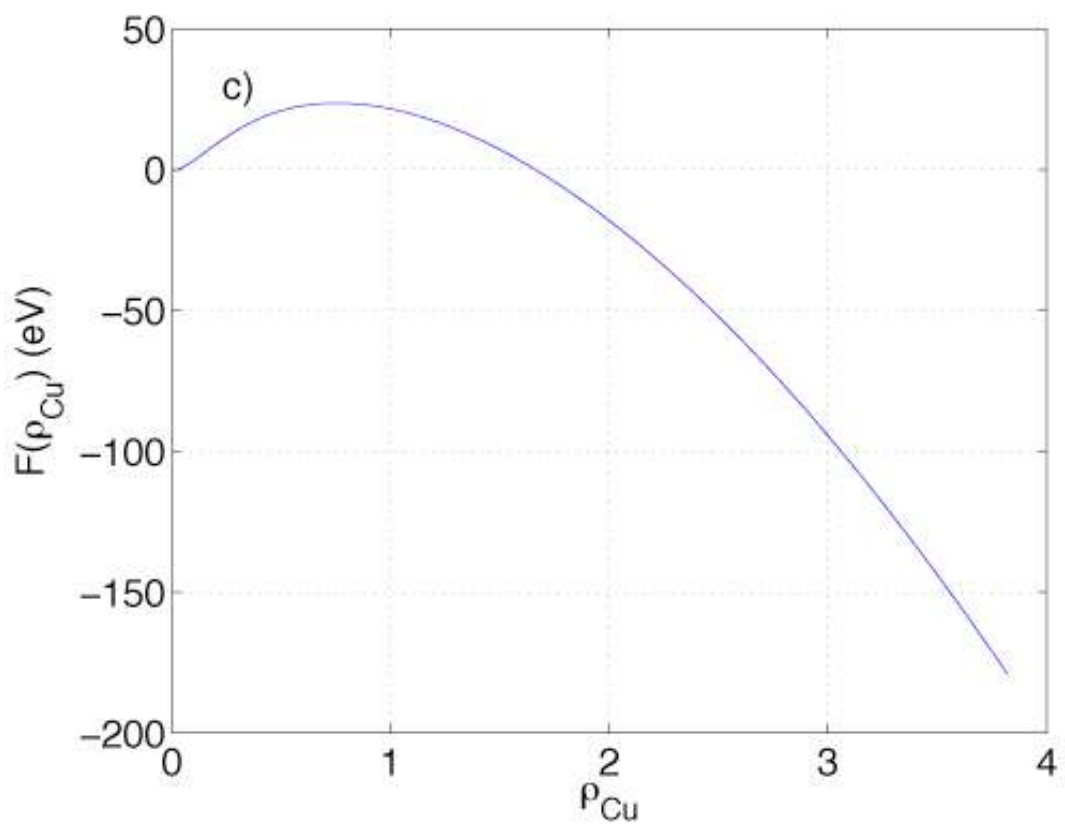
Table IV: Parameters r_a and r_b used in fitting the splines that join the Cu-Nb and ZBL potentials.

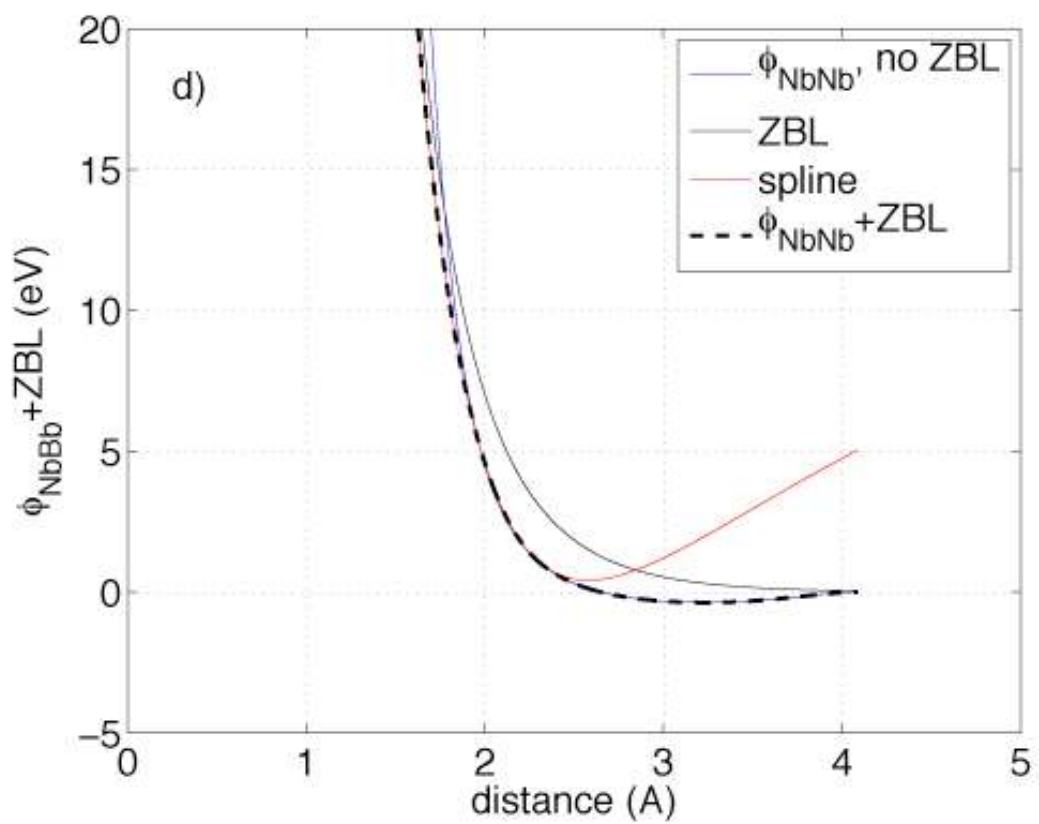
Fitted functions	r_a (Å)	r_b (Å)
$\phi_{\text{CuCu}}(r), \rho_{\text{Cu}}(r)$	1.0	2.0

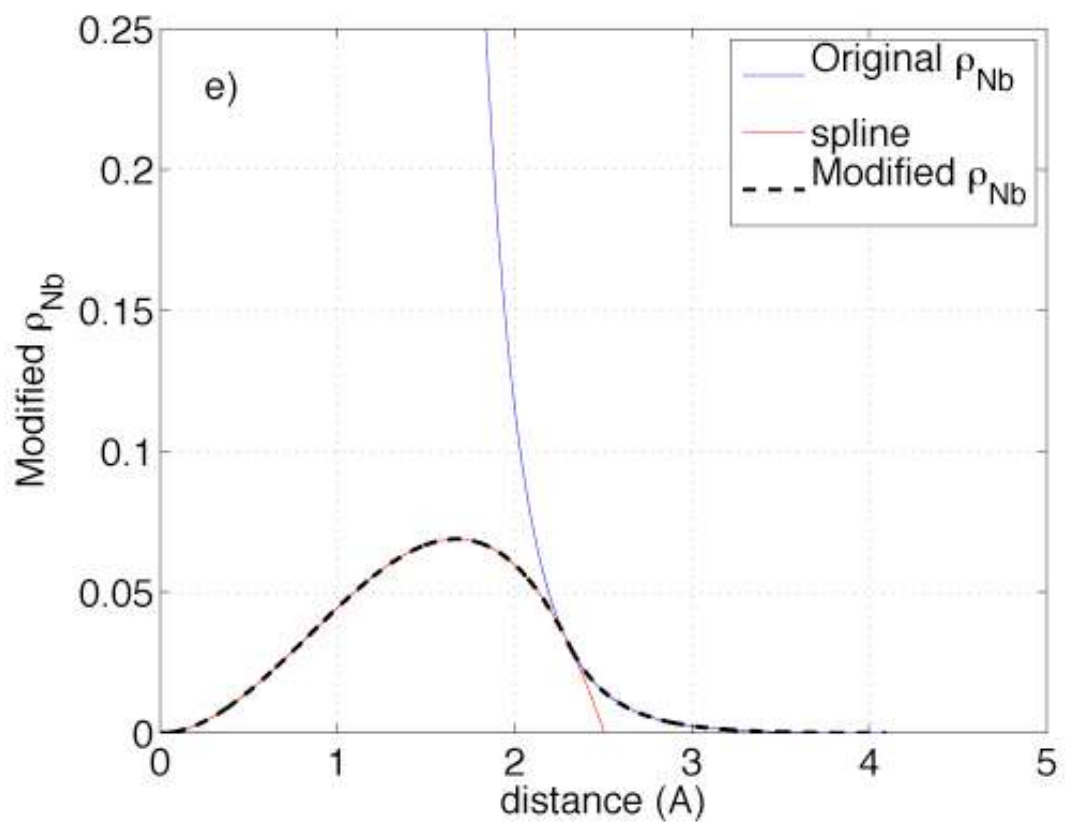
$\phi_{NbNb}(r), \rho_{Nb}(r)$	1.3	2.3
$\phi_{CuNb}(r)$	0.05	2.15

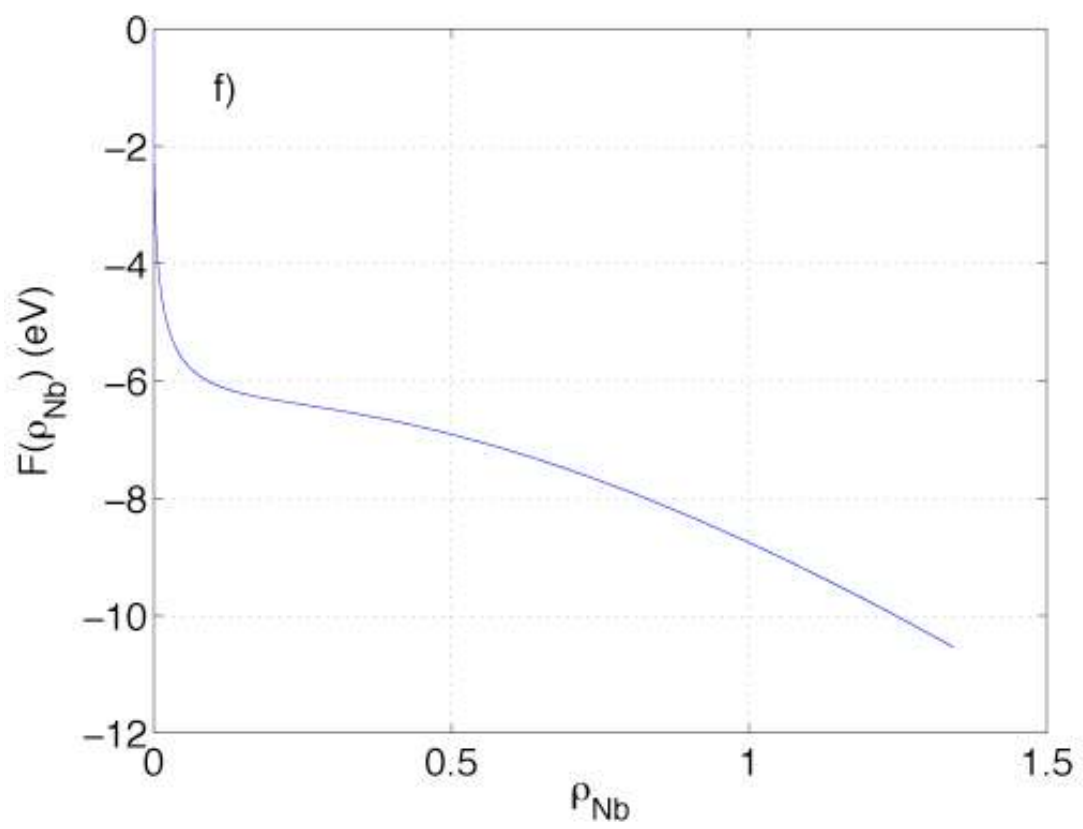












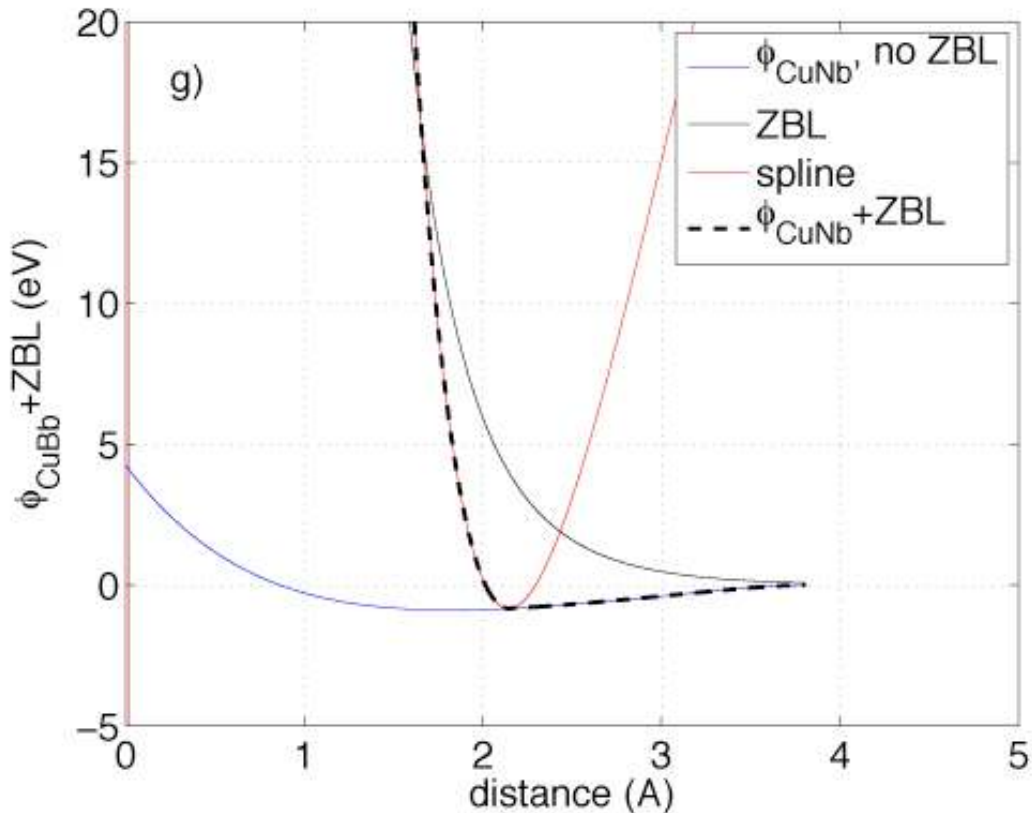


Fig. 2: The functions that define the Cu-Nb+ZBL potential whose construction is described above: a)-c) are for the Cu single-element potential, d)-f) for Nb, and g) for the two-body Cu-Nb interaction.

3. Collision cascade simulations

3.1 Construction of atomic models

The Cu-Nb+ZBL potential described above is used to model collision cascades in fcc Cu, bcc Nb, and in the vicinity of Cu-Nb interfaces formed in the Kurdjumov-Sachs (KS) orientation relation (OR). This orientation relation is the one that has been observed experimentally in sputter deposited Cu-Nb layered nanocomposites [33]. KS interfaces are formed between the close packed planes of neighboring fcc and bcc materials, i.e. $\{111\}$ in Cu and $\{110\}$ in Nb. Within the interface plane, one of the $\langle 110 \rangle$ directions in Cu lies parallel to one of the $\langle 111 \rangle$ directions in Nb.

Figure 3 illustrates how Cu and Nb can be joined in the KS OR. The resulting bilayer model contains one Cu-Nb interface and two free surfaces. Additional interfaces can be created in a single simulation cell by attaching further Cu or Nb slabs in the same OR to the bilayer model. A KS Cu-Nb interface formed between

stress-free Cu and Nb slabs is not periodic, so to impose periodic boundary conditions (PBCs) in the model in Fig. 3 the neighboring Cu and Nb slabs had to be strained slightly along directions parallel to the interface plane. The dimensions of the simulation cell were selected so as to minimize these “periodicity” strains [32].

A remarkable property of Cu-Nb interfaces in the KS OR is that they can exist in a multitude of atomic configurations that are energetically nearly degenerate, though differing by up to several atomic percent in density. This property is primarily a consequence of the geometry of KS Cu-Nb interfaces and not of the details of the potential employed [32]. Examples of different configurations are given elsewhere [4, 34]. For reference, however, we note that when the atomic configuration of the interface plane is that of a perfect $\{111\}$ plane on the Cu side and a perfect $\{110\}$ plane on the Nb (as is the case in Fig. 3) the resulting interface structure has been referred to as KS_1 . This is the configuration that will be used throughout the rest of the work described here. Interfaces formed in other orientation relations or between other pairs of elements might not exhibit the multiplicity of atomic configurations seen in KS Cu-Nb interfaces.

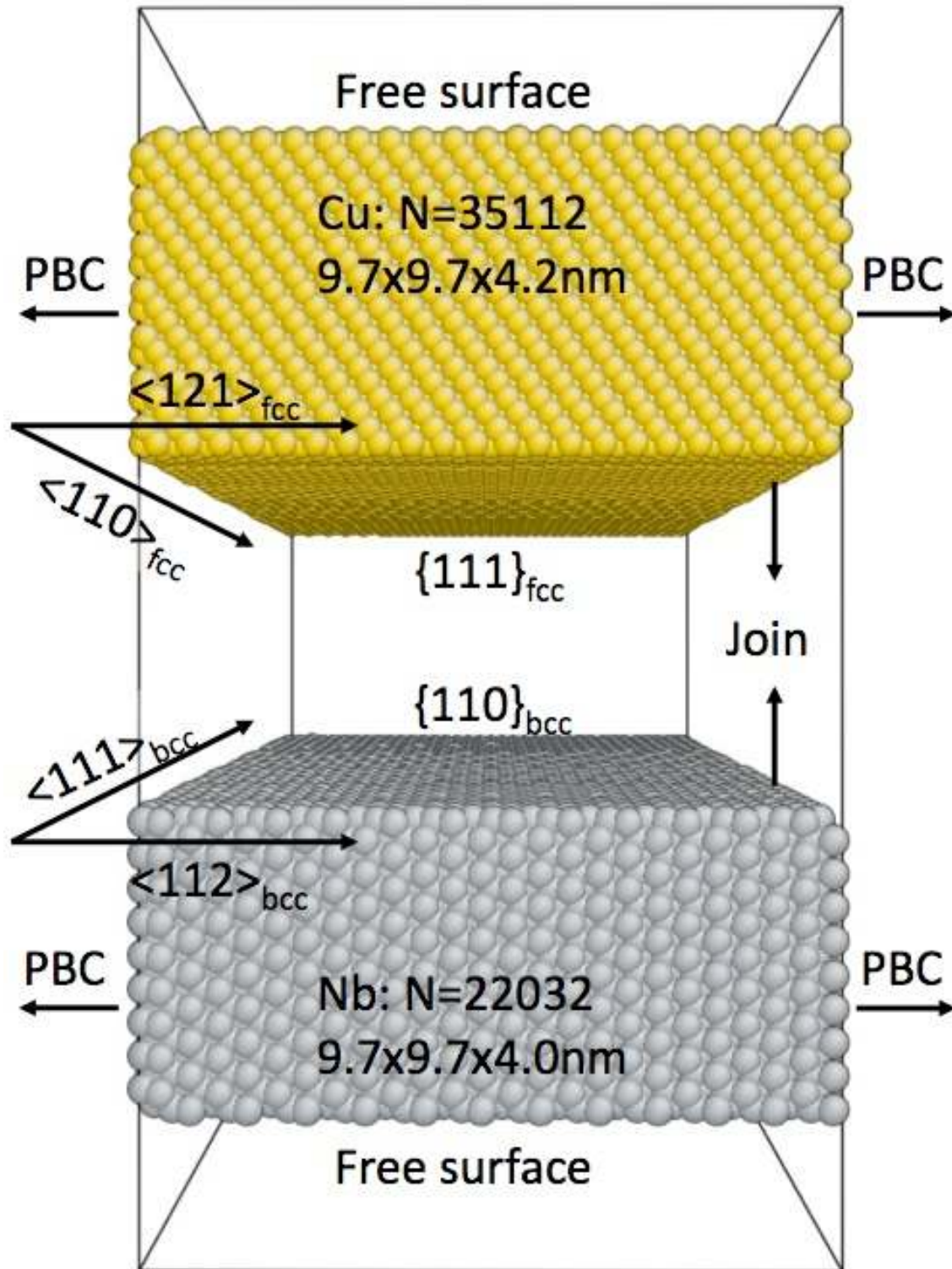


Figure 3: Joining fcc Cu and bcc Nb in the Kurdjumov-Sachs (KS) orientation relation (OR). The model is under periodic boundary conditions (PBCs) along directions parallel to the interface plane and terminates in free surfaces in the direction normal to the interface plane.

In this study, collision cascades were modeled in Cu-Nb-Cu and Nb-Cu-Nb trilayer systems, both constructed by stacking 4nm-thick Cu and Nb crystalline slabs as illustrated in Fig. 3 and each therefore containing two Cu-Nb interfaces. In both systems, each Cu layer contained 35112 and each Nb layer 22032 atoms. Additionally, collision cascades were modeled in perfect fcc Cu and bcc Nb, both under periodic boundary conditions in all three directions. The Cu model consisted of 20x20x20 fcc cubic unit cells and contained 32000 atoms while the Nb model had 25x25x25 bcc cubic unit cells and contained 31250 atoms.

3.2 Modeling primary knock-on events

Cascades were initiated by giving a selected atom—the primary knock-on atom (PKA)—a large kinetic energy well in excess of the thermal mean. This operation is intended to model the transfer of kinetic energy from a swift ion to the PKA during a binary collision. The environments of all atoms in the periodic perfect fcc Cu and bcc Nb models are equivalent, so PKAs and the directions of their velocities were selected at random in these systems. In the Cu-Nb-Cu and Nb-Cu-Nb models PKAs were selected from the central layer. If Nb {110} planes parallel to Cu-Nb interfaces are numbered beginning with plane “one” lying directly at a Cu-Nb interface, PKAs were chosen either from the second or ninth Nb {110} atomic planes, corresponding to distances of 3.5Å or 22.2Å from the nearest Cu-Nb interface, respectively. Similarly, PKAs in Cu were chosen from either the second or eleventh Cu {111} planes, i.e. 3.2Å or 24.0Å from the nearest Cu-Nb interface. PKA velocities in the trilayer systems were directed towards the closest interface, with randomly selected deviations from the interface normal, not exceeding 8 degrees.

Kinetic energies given to PKAs were chosen to be representative of He implantation experiments carried out on Cu-Nb multilayer nanocomposites [1-3, 6], where the energy of the implanted ions was 33keV. The SRIM Monte Carlo program [35] was used to investigate the distribution of PKA energies for this implantation energy and the results are shown in Fig. 4. Two types of binary collisions were investigated: recoil and replacement collisions. The former is a glancing (large impact parameter [36]) collision after which both the PKA and the implanted ion depart from the location where the collision occurred. The latter is a “head-on” (low impact parameter) collision after which the implanted ion remains in the vacancy created by the departing PKA. Recoil collisions occur about five times more frequently than replacement collisions, as illustrated in Figs 4.a) and 4.b). On the other hand, the mean kinetic energy transferred during a replacement collision from an impacting ion of given energy is about twice as high as that transferred during a recoil collision, as shown in Figs 4.c) and 4.d).

Figure 4.d) demonstrates that PKA energies larger than about 2.5keV are unlikely for the 33keV He ions used in the Cu-Nb nanocomposite implantation

experiments. Thus, to obtain a representative sampling of the collision-induced damage sustained under these conditions we conducted collision cascade simulations with PKA energies ranging from 0.5 to 2.5keV in increments of 0.5keV. Two cascades at each PKA energy were carried out in all four systems described above. For a given PKA energy in the trilayer systems, one of the simulations was conducted with a PKA in the second atomic plane from the nearest Cu-Nb interface and the other simulation was conducted with a PKA chosen from the more distant atomic plane (the 9th in Nb, the 11th in Cu).

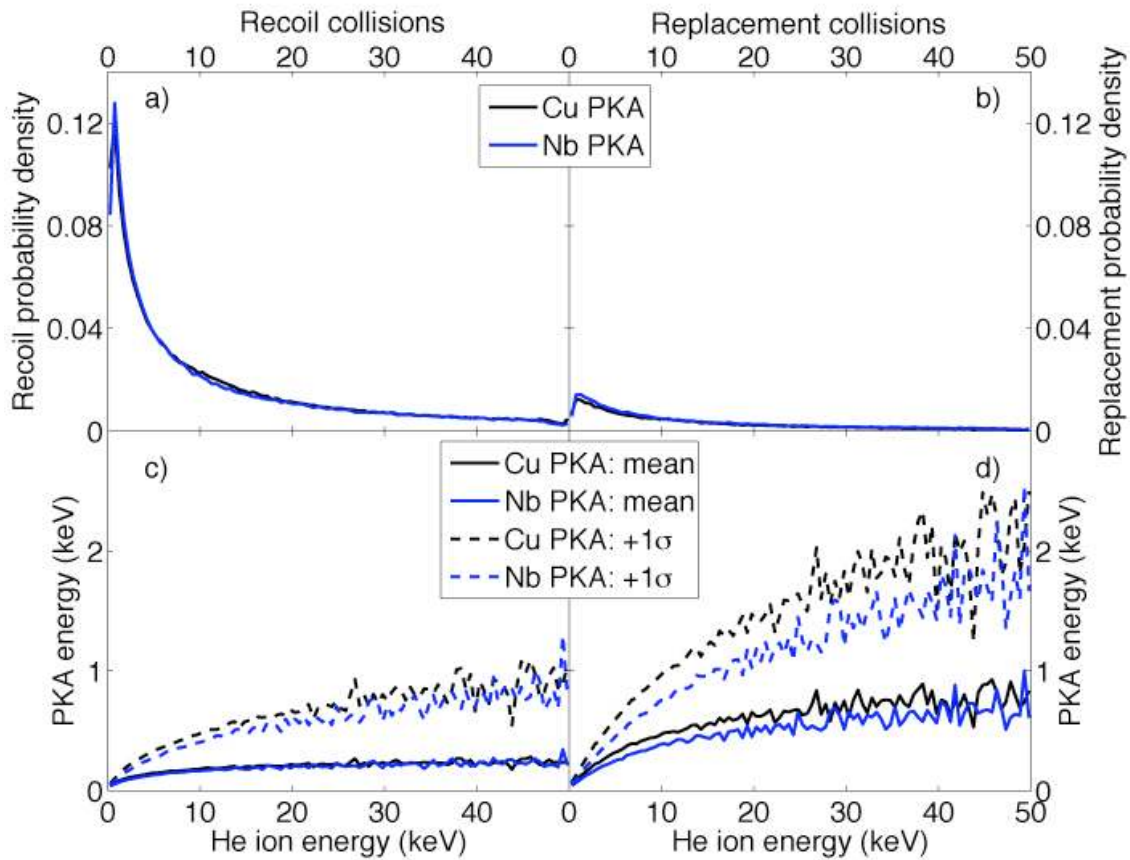


Fig. 4: The probability of occurrence of recoil and replacement collisions between implanted He atoms and Cu or Nb primary knock-on atoms (PKAs) in the target lattice are shown in a) and b), respectively. The kinetic energies transferred to the PKAs as a function of the energy of the implanted ions are plotted for recoil and replacement collisions in c) and d), respectively. Solid lines represent the mean PKA energy while the dashed lines demarcate the envelope of 1 standard deviation away from the mean.

3.3 Conduct and analysis of cascade simulations

Before collision cascades were initiated, each system was thermalized for 60ps at 100K and zero total pressure. Velocity rescaling [37] and the Anderson barostat [38] with damping were used to control the temperature and pressure, respectively. Next, a collision cascade was initiated by giving the selected PKA a kinetic energy from the spectrum discussed in subsection 3.2. The system was then allowed to evolve at constant energy and simulation cell shape for 1.5ps. Because during this stage of the simulation atoms approach each other to distances where the forces between them vary rapidly with separation, accurate integration of the atomic trajectories requires a time step that may be much shorter than one that would have sufficed under conditions of thermal equilibrium. To ensure both accuracy and efficiency, the Gear predictor-corrector [37] with a variable time step was applied. The time increment Δt used for integration was chosen to have the greatest value that satisfied the following three criteria:

- $\Delta t \leq 3\text{fs}$
- For every atom i (with speed $|\vec{v}_i|$), $|\vec{v}_i| \cdot \Delta t \leq 0.1\text{\AA}$
- For every atom i (with velocity \vec{v}_i and net force \vec{f}_i), $|\vec{v}_i \cdot \vec{f}_i| \cdot \Delta t \leq 2\text{eV}$

With this approach, time steps Δt as small as 7.55zs ($7.55 \cdot 10^{-21}\text{s}$) were used, but the number of integration steps necessary to perform the entire 1.5ps simulation never exceeded 136000 and the energy drift due to integration inaccuracy was about 0.3eV/ps.

The post-collision cascade atomic configurations were further annealed at constant temperature ($T=300\text{K}$) and simulation cell shape for 75ps and finally quenched to zero temperature by conjugate gradient minimization of the potential energy [30]. Visualizations of fcc Cu, bcc Nb, and Cu-Nb interfaces in typical end states are shown in Fig. 5. In these figures, atomic environments have been analyzed using common neighbor analysis (CNA) [39, 40] and all atoms with perfect fcc or bcc environments were removed for clarity. The remaining atoms neighbor on Cu-Nb interfaces or on defects remaining from collision cascades.

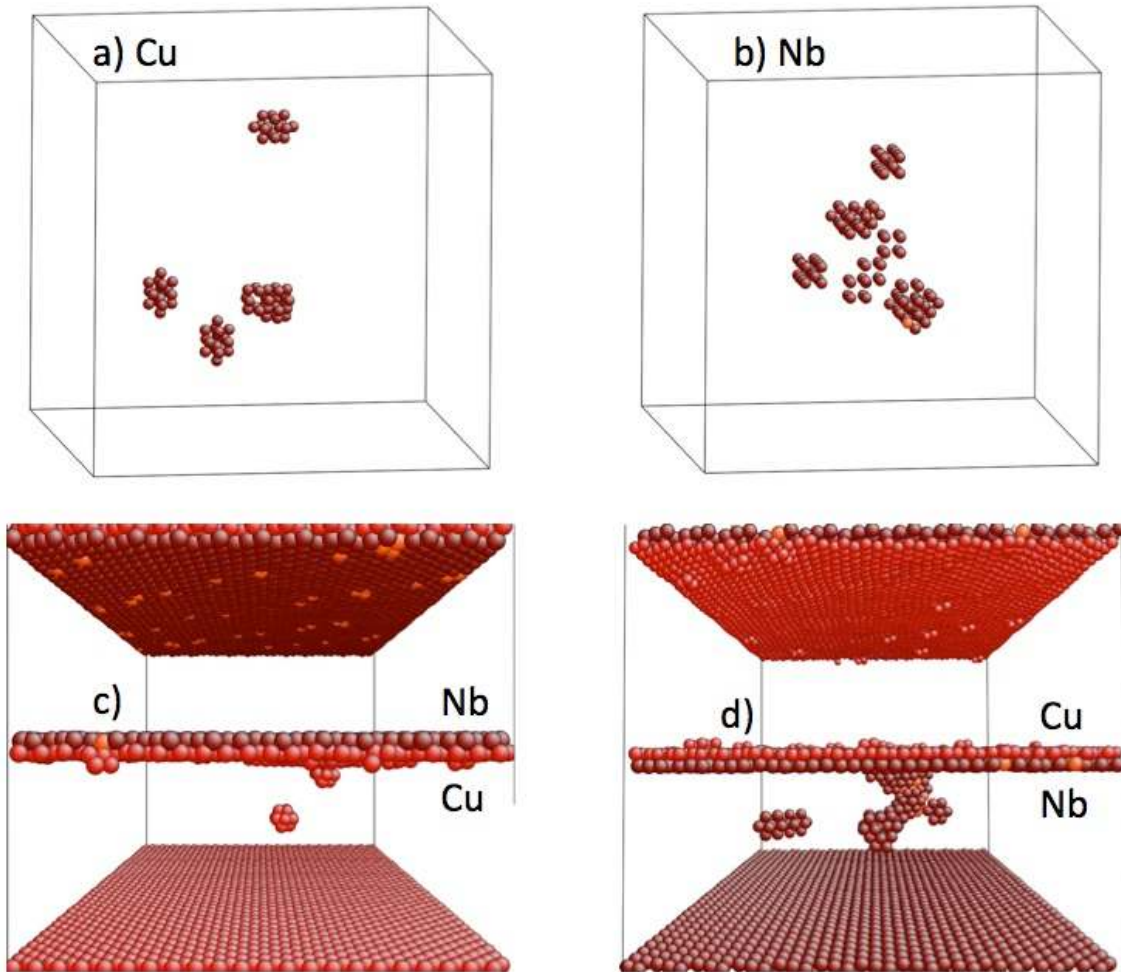


Fig. 5: Representative damage states after 1.0 keV PKA collision cascades: a) fcc Cu, b) bcc Nb, c) Cu-Nb interface with PKA from the Nb layer, d) Cu-Nb interface with PKA from the Cu layer. Atomic environments were characterized using common neighbor analysis. No atoms with perfect fcc or bcc environments are shown.

For the PKA energies used in this work, the defects remaining after collision cascades in fcc Cu and bcc Nb could be identified by inspection and counted. On the other hand, the defect configurations remaining after collision cascades in the trilayer systems were often difficult to characterize. In addition to isolated vacancies and interstitials, substitutionals and clusters thereof were observed, as were complex interface reconstructions. In the following, we will compare the number of Frenkel pairs remaining in fcc Cu and bcc Nb to the number of vacancies and self-interstitials found far enough away from Cu-Nb interfaces in the trilayer systems to be identified as conventional point defects. Note that unlike in pure Cu and Nb, the number of vacancies and interstitials found in the trilayer systems need not be equal because in each simulation a different number of these defects may have been

trapped at Cu-Nb interfaces. The number of substitutionals created during collision cascades is also reported.

In models of irradiation-induced defect creation such as that of Kinchin and Pease [36] the average number of collision cascade-induced defects rises as a linear function of PKA energy if that energy is above the Frenkel pair creation threshold (typically $<100\text{eV}$) and below the energy at which the incoming ions are slowed primarily by electronic excitations (which can be approximated as the atomic mass number of the ion times 1keV [41]). Because all the PKA energies used in this study fall within this linear range, the collision cascade-induced defect production is reported in table V as the number of defects produced per keV of PKA energy. This quantity was obtained using a linear least squares fit of the number of defects produced at different PKA energies.

Table V: Collision cascade-induced damage in fcc Cu, bcc Nb, and in Cu-Nb systems reported as number of defects produced per keV of PKA energy.

Damage type	Damage/PKA energy (#/keV)
Frenkel pairs in fcc Cu	2.0
Frenkel pairs in bcc Nb	3.2
vacancies in Cu-Nb systems	1.0
interstitials in Cu-Nb systems	1.1
substitutionals in Cu-Nb systems	6.3

These results demonstrate a reduction of between 50-70% in the number of vacancies and interstitials created near Cu-Nb interfaces compared to the number formed in fcc Cu and bcc Nb. Thus, Cu-Nb interfaces are able to remove a sizeable fraction of collision cascade-induced point defects within the lifetime of the cascades themselves. A dramatic instance of this effect was observed in one particular cascade in a Nb-Cu-Nb trilayer with PKA energy of 1.5keV . The development of the cascade is illustrated in Fig. 6. The PKA starts out in the middle of a Cu layer [Fig. 6.a)] and creates defects as it dissipates its kinetic energy through collisions with other atoms [Fig. 6.b)]. Within 1ps , however, the cascade core size rapidly shrinks as defects are trapped and recombined at the Cu-Nb interface [Fig. 6.c)]. No defects remain 2ps after the beginning of the cascade and the crystalline Cu and Nb layers are flaw-free [Fig. 6.d)]. In Fig. 6, atoms are characterized by their “local excess energy,” defined as the atom kinetic energy plus the atomic contribution to potential energy minus the cohesive energy of the atom type (Cu or Nb, as appropriate). Atoms with local excess energies less than 0.7eV are not shown, leaving only those with high velocities or defective atomic environments.

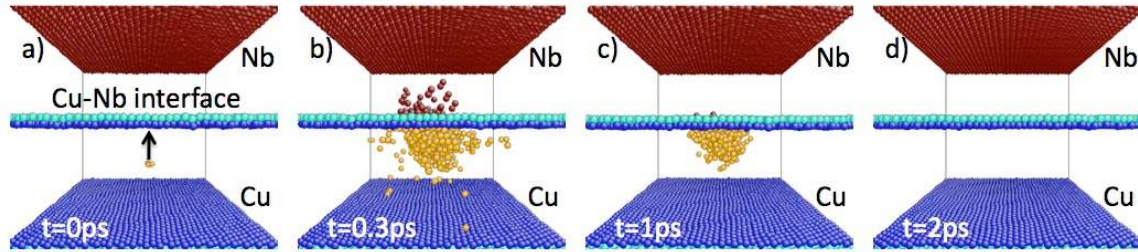


Fig. 6: The progress of a 1.5keV PKA collision cascade in a Nb-Cu-Nb trilayer illustrates the ability of Cu-Nb interfaces to trap and recombine irradiation-induced defects. In a), the arrow indicates the initial direction of the PKA.

Unlike in pure fcc Cu and bcc Nb, substitutional defects can form in Cu-Nb multilayer systems. Their number is substantially larger than the number of collision cascade-induced vacancies or interstitials. Because Cu and Nb are immiscible, these substitutionals will tend to de-mix over time. The proportion of the rate of de-mixing to the implantation dose rate will likely play an important role in determining the limits of morphological stability of irradiated multilayer composites.

4. Discussion

We have described the construction of an EAM Cu-Nb potential by the joining of single-element Cu and Nb EAM potentials. Because the inter-element interactions were modeled by fitting low energy, thermal equilibrium properties (like dilute enthalpies of mixing) such potentials may not model high-energy atomic collisions well. Therefore, we also developed a method for porting the ZBL universal short-range repulsive potential to the Cu-Nb EAM potential. We have also found that although it is possible to find many different parameterizations of the Cu-Nb potential, some of them may predict deep, unphysical energy minima at low interatomic separations and should be rejected in favor of those that do not. In view of this finding, we recommend that investigation of behavior at low atomic separations should become standard practice in the construction of any multi-element potential from single element potentials.

The Cu-Nb-ZBL potential developed here was used to conduct collision cascade simulations in fcc Cu, bcc Nb, and in the vicinity of Cu-Nb interfaces in the Kurdjumov-Sachs (KS) orientation relation. By absorbing and recombining collision cascade-induced defects, Cu-Nb interfaces reduce the number of vacancies and interstitials produced per keV of primary knock-on atom (PKA) energy by 50-70% compared to fcc Cu or bcc Nb. In relating these simulations to experiments it should be remembered that no electronic processes were taken into account in our model. Stopping by direct electronic excitations is unlikely to contribute significantly to damping the motion of atoms for the PKA energies considered here [41], but the

omission of electronic contributions to thermal conductivity may give rise to an underprediction of the rate of quenching of cascade cores, leading to reduced defect survival probability in our simulations. This effect, however, would be expected for collision cascades in both the perfect crystalline (fcc Cu and bcc Nb) systems as well as in the Cu-Nb-Cu and Nb-Cu-Nb trilayers. We therefore expect that our conclusion that Cu-Nb interfaces reduce the number of cascade-induced vacancies and interstitials *as compared* with the behavior of perfect crystalline Cu and Nb will be unaffected by the omission of electronic contributions to thermal conductivity. Furthermore, previous investigations [34] have shown that energy barriers for migration to Cu-Nb interfaces vanish for point defects at distances to Cu-Nb interfaces comparable to the distances at which PKAs were chosen in the present work. Thus, faster quenching of cascade cores is less likely to affect the defect survival probability in the vicinity of Cu-Nb interfaces than in crystalline Cu or Nb, making the 50-70% reduction in defect concentration determined in this study a lower bound on the actual reduction.

This study also identified several avenues for improving the atomistic modeling of radiation effects in Cu-Nb composites. First, the Nb single element EAM potential used here (see Appendix A) has since been superseded by one that better models the behavior of interstitial defects in Nb [42] and should be used in future parameterizations of Cu-Nb two-element potentials. The properties of mixed interstitials should also be considered in fitting next-generation Cu-Nb two-element potentials. Second, collision cascade simulations revealed considerable complexity in the response of Cu-Nb interfaces to energetic ion bombardment. A robust classification of the collision-induced defects found there should be developed, as should automated methods for their characterization and classification. Such tools will enable more exhaustive and informative collision cascade simulations to be carried out in the future. Finally, the morphological stability of interfaces in irradiated nanocomposites over time scales much longer than those accessible to conventional molecular dynamics studies may be influenced by the variety and complexity of interface responses to collision cascades. How these long time scales can be accessed in atomistic simulations remains an open question.

Appendix A: Single-element EAM Cu and Nb potentials

Here we describe the single-element Cu and Nb potentials that were used in creating the two-element Cu-Nb EAM potential. As stated in section 2, the Cu potential was created by Voter [18] (we describe it here for completeness' sake) and the Nb potential was constructed using the form introduced by Johnson and Oh [21].

The two-body interaction in the Cu potential is of the Morse form

$$\phi_{CuCu}(r) = D_M \left(1 - e^{-\alpha_M(r-R_M)}\right)^2 - D_M \quad (11)$$

while the electron density contribution from any given Cu atom has the form of a 4s hydrogenic electron orbital

$$\rho_{Cu}(r) = r^6 \cdot \left(e^{-\beta r} + 2^9 e^{-2\beta r}\right). \quad (12)$$

The two-body interaction is modified so that its value and the value of its first derivative go smoothly to zero at a specified cutoff radius r_{cut} :

$$\phi'_{CuCu}(r) = \phi_{CuCu}(r) - \phi_{CuCu}(r_{cut}) + \frac{r_{cut}}{20} \left(1 - r^{20}/r_{cut}^{20}\right) \frac{d\phi_{CuCu}}{dr} \Big|_{r=r_{cut}}. \quad (13)$$

The electron density function in eqn. 12 is also modified according to this scheme. In eqn.s 11-13, r stands for an interatomic distance and all other symbols— D_M , α_M , R_M , β , r_{cut} —are parameters that can be adjusted to optimize the ability of the potential to reproduce selected properties of Cu.

With $\phi_{CuCu}(r)$ and $\rho_{Cu}(r)$ specified, the form of the embedding function $F_{Cu}(\bar{\rho})$ can be chosen to make the total energy of perfect fcc Cu follow the universal binding energy relation (UBER) of Rose et al. [43] exactly. This is accomplished by numerically determining $F_{Cu}(\bar{\rho})$ such that eqn. 1 is always obeyed for an fcc lattice in varying states of dilatation or contraction when the total energy of the system is fixed by $V = N \cdot E_U(a)$, where N is the number of atoms and $E_U(a)$ the energy per atom at lattice constant a predicted by the UBER.

The UBER expresses E_U for given values of the cubic lattice constant a is

$$E_U(a^*) = -E_{coh} f(a^*) \quad (14)$$

$$f(a^*) = (1 + a^*)e^{-a^*}$$

$$a^* = (a/a_0 - 1) / \sqrt{E_{coh}/9B\Omega}$$

where a_0 is the equilibrium lattice constant, E_{coh} the cohesive energy, B the bulk modulus, and Ω the volume per atom. These quantities are reproduced by construction when $F_{Cu}(\bar{\rho})$ is chosen such that the UBER is followed. Because the Cu EAM potential imposes a finite range on atomic interactions (as reflected by the cutoff in functions $\phi_{CuCu}(r)$ and $\rho_{Cu}(r)$ shown in eqn. 13) the embedding function $F_{Cu}(\bar{\rho})$ is in fact chosen to reproduce a slightly modified form of the UBER where

$$f_{mod}(a^*) = \frac{f(a^* \sqrt{1-\varepsilon}) - \varepsilon}{1 - \varepsilon} \quad (15)$$

and the parameter ε is chosen to make E_U exactly zero at the lattice parameter a_{cut} at which the nearest neighbor distances reach the cutoff distance r_{cut} . In the final form of this Cu EAM potential, $\varepsilon \approx 0.0506$.

The values of the fitting parameters D_M , α_M , R_M , β , and r_{cut} are chosen by minimizing the RMS deviation between the values of the cubic elastic constants C_{11} , C_{12} , C_{44} , the unrelaxed vacancy formation energy ΔE_v , and the Cu-Cu dimer energy E_d and separation r_d predicted by the Cu EAM potential and the corresponding experimentally determined values. Table VI lists the final values of the fitting parameters while table VII compares the resulting calculated C_{11} , C_{12} , C_{44} , ΔE_v , E_d , and r_d to their target experimental values.

Table VI: Values of the fitting parameters entering into the expressions in eqn.s 11-13 for the Cu EAM potential.

Parameter	D_M (eV)	R_M (Å)	α_M (Å ⁻¹)	β_M (Å ⁻¹)	r_{cut} (Å)
Value	0.7366	2.3250	1.9190	4.0430	4.9610

Table VII: Comparison of physical quantities calculated with the Cu EAM potential to the target experimentally determined values. The potential reproduces by construction the quantities marked with asterisks.

Quantity	a_0 (Å)	E_{coh} (eV)	B (GPa)	C_{11} (GPa)	C_{12} (GPa)	C_{44} (GPa)	ΔE_v (eV)	E_d (eV)	R_d (Å)
EAM Cu	*	*	*	179	123	81	1.3	2.07	2.23
Experiment	3.615 [44]	3.54 [45]	142 ^a	176 ^a	125 ^a	82 ^a	1.3 [46]	2.05 ^b	2.2 ^b

^a[47], ^b[48]

One of the distinct successes of the EAM Cu potential constructed by Voter as described above is that it predicts the correct lowest-energy self-interstitial configuration (the 100-split dumbbell) with formation energy and volume in good agreement with experimentally determined values [49]. It must be emphasized that self-interstitial properties were not used in the fitting procedure. The physical origin of this success may be ascribed to having required the potential to reproduce the UBER and to having included the Cu-Cu dimer energy and separation among the fitted quantities. Both of these ingredients contribute information about the energetics of the Cu system for the small interatomic separations characteristic of the environment of an interstitial. These separations are several tenths of Angstroms below the equilibrium fcc Cu-Cu nearest neighbor distance and are not probed by the other fitted quantities (a_0 , E_{coh} , B , C_{11} , C_{12} , C_{44} , ΔE_v).

We have attempted to use the above method to construct an EAM potential for Nb, but without success. We therefore adopted the form of EAM potentials designed specifically for bcc metals by Johnson and Oh [21]. In it, the pair interaction is given by

$$\phi_{NbNb}(r) = K_1 \cdot \left(\frac{r}{r_s} - 1 \right) + K_2 \cdot \left(\frac{r}{r_s} - 1 \right)^2 + K_3 \cdot \left(\frac{r}{r_s} - 1 \right)^3, \quad (16)$$

the contribution to electron density due to any given Nb atom by

$$\rho_{Nb}(r) = \left(\frac{r_s}{r} \right)^\beta, \quad (17)$$

and the embedding energy by

$$F_{Nb}(\bar{\rho}) = F_e \bar{\rho}^n \cdot (1 - \log \bar{\rho}^n). \quad (18)$$

The pair interaction ϕ_{NbNb} is modified so that its value and that of its first derivative approach zero at a specified cutoff radius r_{cut} by using the following formula:

$$\phi'_{NbNb}(r) = \phi_{NbNb}(r) - \phi_{NbNb}(r_{cut}) + \left(\frac{r_{cut} - r_s}{7}\right) \cdot \left[1 - \left(\frac{r - r_s}{r_{cut} - r_s}\right)^7\right] \frac{d\phi_{NbNb}}{dr} \Big|_{r=r_{cut}}. \quad (19)$$

The electron density function ρ_{Nb} is similarly modified using

$$\rho'_{Nb}(r) = \rho_{Nb}(r) - \rho_{Nb}(r_{cut}) + \frac{r_{cut}}{7} \left(1 - r^7/r_{cut}^7\right) \frac{d\rho_{Nb}}{dr} \Big|_{r=r_{cut}}. \quad (20)$$

Parameters K_1 , K_2 , K_3 , β , F_0 , n , r_s , and r_{cut} in eqn.s 16-20 can be adjusted to optimize the performance of the potential. This is done by a method similar to the one described in subsection 2.2 for fitting the Cu-Nb interaction. Namely, the simplex method [30, 31] is used to minimize an objective function written as a sum of the squares of deviations of physical quantities calculated using the potential from experimentally determined values. The quantities that were fitted are the three independent cubic elastic constants C_{11} , C_{12} , and C_{44} , the equilibrium lattice parameter a_0 and cohesive energy E_{coh} of bcc Nb, the difference in cohesive energy between Nb in the bcc and fcc structures $\Delta E_{bcc-fcc}$, and the relaxed vacancy formation energy in bcc Nb ΔE_v . Table VIII lists the final values of the potential parameters while table IX compares the calculated and experimentally determined values of the physical quantities used in the fitting.

Table VIII: Values of the fitting parameters entering into the expressions in eqn.s 16-20 for the Nb EAM potential.

Parameter	K_1 (eV)	K_2 (eV)	K_3 (eV)	β	F_0 (eV)	n	r_s (Å)	r_{cut} (Å)
Value	-0.671	3.524	3.651	9.084	4.709	0.463	2.853	4.087

Table IX: Comparison of physical quantities calculated with the Nb EAM potential to the target experimentally determined values.

Quantity	C_{11} (GPa)	C_{12} (GPa)	C_{44} (GPa)	a_0 (Å)	E_{coh} (eV)	$\Delta E_{bcc-fcc}$ (eV)	ΔE_v (eV)
EAM Nb	245.8	133.8	28.8	3.3008	7.47	0.2902	2.70
Experiment	247.6 ^a	149.0 ^a	27.5 ^a	3.3008	7.47	0.0932	2.75
				[50]	[51]	[21]	[52, 53]

^a[47]

Although the EAM potential described above successfully reproduces the bcc crystal structure of Nb as well as the physical quantities used in the fitting procedure, it does not achieve the same success in predicting the correct self-interstitial properties: contrary to the findings of first principles calculations [54], it gives the 100-split dumbbell rather than the 111-split dumbbell as the lowest energy interstitial structure. Furthermore, at 3.11 eV the lowest self-interstitial formation energy predicted by this potential is about 2 eV too low. These shortcomings may be ascribed to the fact that none of the fitted physical quantities listed in Table IX probe the energetics of Nb-Nb interaction for interatomic separations markedly smaller than the Nb bcc equilibrium nearest neighbor distance. Approaches that model these short-range interactions [42] should therefore be adopted in the future.

Appendix B: Ziegler-Biersack-Littmark model for interatomic repulsive forces

During collisions occurring in irradiated solids, atoms approach each other to distances that are shorter—possibly by orders of magnitude, depending on the collision energy—than the shortest distances arising from purely thermal agitation. At such small separations, atoms are strongly repelled due to electrostatic interactions between the atom nuclei as well as the overlapping core electron distributions. The resulting interatomic forces have been studied by Ziegler, Biersack, and Littmark, who formulated an effective potential for atomic repulsion [35]. This potential—called “ZBL” after the authors—is sometimes referred to as “universal” in the sense that the potential energy curves for any pair of atoms at short separation collapse to the ZBL description given appropriate scaling of distances by the atomic numbers of the colliding atoms, as summarized below. The ZBL potential may be viewed as a high-energy analog of the Universal Binding Energy Relation (UBER) of Rose and co-workers [43], which demonstrates that curves of cohesive energy vs. lattice parameter may be collapsed to one “universal” curve given the appropriate scaling of the lattice parameter. Comparison of the ZBL potential and other descriptions of short-range repulsive forces with first-principles calculations demonstrates the superior accuracy of the ZBL potential [55].

For a pair of atoms with atomic numbers Z_1 and Z_2 separated by a distance r the ZBL potential can be written

$$V(r) = \left(\frac{Z_1 Z_2 e^2}{r} \right) \Phi(r) \quad (21)$$

where e is the elementary charge and

$$\Phi(r) = 0.1818e^{-3.2r/a_U} + 0.5099e^{-0.9423r/a_U} + 0.2802e^{-0.4028r/a_U} + 0.02817e^{-0.2016r/a_U}. \quad (22)$$

The scaling constant a_U is expressed as

$$a_U = \frac{c_{TF}a_0}{Z_1^{0.23} + Z_2^{0.23}} \quad (23)$$

where $c_{TF} = \frac{1}{2} \left(\frac{3\pi}{4} \right)^{2/3} \approx 0.8853$ is a constant in the Thomas-Fermi model of screened interactions [36] and $a_0 \approx 0.529\text{\AA}$ is the Bohr radius.

Acknowledgements

We thank S. G. Srivilliputhur for performing the VASP calculations used in this work and to M. I. Baskes, P. M. Derlet, and S. M. Valone for useful discussions. This work was funded by the LANL Laboratory Directed Research and Development (LDRD) Program and a LANL Director's Postdoctoral Fellowship.

References

- [1] T. Hochbauer, A. Misra, K. Hattar, and R. G. Hoagland, *J. Appl. Phys.* **98** (2005) 123516.
- [2] X. Zhang, N. Li, O. Anderoglu, H. Wang, J. G. Swadener, T. Hochbauer, A. Misra, and R. G. Hoagland, *Nucl. Inst. Meth. B* **261** (2007) 1129.
- [3] A. Misra, M. J. Demkowicz, X. Zhang, and R. G. Hoagland, *JOM* **59** (2007) 62.
- [4] M. J. Demkowicz, R. G. Hoagland, and J. P. Hirth, *Phys. Rev. Lett.* **100** (2008) 136102.
- [5] M. J. Demkowicz, Y. Q. Wang, R. G. Hoagland, and O. Anderoglu, *Nucl. Inst. Meth. B* **261** (2007) 524.
- [6] K. Hattar, M. J. Demkowicz, A. Misra, I. M. Robertson, and R. G. Hoagland, *Scripta Mater.* **58** (2008) 541.
- [7] A. Misra, R. G. Hoagland, and H. Kung, *Phil. Mag.* **84** (2004) 1021.
- [8] R. S. Averback, D. Peak, and L. J. Thompson, *Appl. Phys. A* **39** (1986) 59.

- [9] L. U. Aaen Andersen, J. Bottiger, and K. Dyrbye, *Mater. Sci. Eng. A* **115** (1989) 123.
- [10] R. G. Hoagland, J. P. Hirth, and A. Misra, *Phil. Mag.* **86** (2006) 3537.
- [11] A. Misra, M. J. Demkowicz, J. Wang, and R. G. Hoagland, *JOM* **60** (2008) 39.
- [12] M. S. Daw and M. I. Baskes, *Phys. Rev. B* **29** (1984) 6443.
- [13] M. I. Baskes, *Phys. Rev. B* **46** (1992) 2727.
- [14] M. I. Baskes, S. G. Srinivasan, S. M. Valone, and R. G. Hoagland, *Phys. Rev. B* **75** (2007) 094113.
- [15] D. G. Pettifor, *Phys. Rev. Lett.* **63** (1989) 2480.
- [16] D. G. Pettifor and Oleinik, II, *Phys. Rev. B* **59** (1999) 8487.
- [17] Oleinik, II and D. G. Pettifor, *Phys. Rev. B* **59** (1999) 8500.
- [18] A. F. Voter, LANL Unclassified Technical Report # LA-UR 93-3901 (1993)
- [19] S. M. Foiles, M. I. Baskes, and M. S. Daw, *Phys. Rev. B* **33** (1986) 7983.
- [20] R. A. Johnson, *Phys. Rev. B* **37** (1988) 3924.
- [21] R. A. Johnson and D. J. Oh, *J. Mater. Res.* **4** (1989) 1195.
- [22] A. F. Voter and S. P. Chen, *Mater. Res. Soc. Symp. Proc.* **82** (1987) 175.
- [23] D. Udler and D. N. Seidman, *Interface Sci.* **3** (1995) 41.
- [24] A. F. Voter, in Intermetallic Compounds: Principles and Practice, Vol. 1 (J. H. Westbrook and R. L. Fleischer, eds.), John Wiley & Sons, New York, 1994, p. 77.
- [25] M. I. Baskes and C. F. Melius, *Phys. Rev. B* **20** (1979) 3197.
- [26] M. S. Daw, S. M. Foiles, and M. I. Baskes, *Mater. Sci. Rep.* **9** (1993) 251.
- [27] L. Kaufman, *CALPHAD* **2** (1978) 117.
- [28] G. Kresse and J. Hafner, *Phys. Rev. B* **47** (1993) 558.
- [29] G. Kresse and D. Joubert, *Phys. Rev. B* **59** (1999) 1758.
- [30] D. P. Bertsekas, Nonlinear Programming, Athena Scientific, Cambridge, MA, 1999.
- [31] T. Rowan, Ph.D. thesis, University of Texas at Austin, 1990.
- [32] M. J. Demkowicz and R. G. Hoagland, *J. Nucl. Mater.* **372** (2008) 45.
- [33] P. M. Anderson, J. F. Bingert, A. Misra, and J. P. Hirth, *Acta Mater.* **51** (2003) 6059.
- [34] M. J. Demkowicz, J. Wang, and R. G. Hoagland, in Dislocations in Solids, Vol. 14 (J. P. Hirth, ed.), Elsevier, Amsterdam, 2008, p. 141.
- [35] J. F. Ziegler, J. P. Biersack, and U. Littmark, The stopping and range of ions in solids, Pergamon, New York, 1985.
- [36] M. A. Nastasi, J. W. Mayer, and J. K. Hirvonen, Ion-solid interactions: fundamentals and applications, Cambridge University Press, Cambridge, 1996.
- [37] M. P. Allen and D. J. Tildesley, Computer Simulation of Liquids, Oxford University Press, Oxford, 1987.
- [38] H. C. Andersen, *J. Chem. Phys.* **72** (1980) 2384.
- [39] J. D. Honeycutt and H. C. Andersen, *J. Phys. Chem.* **91** (1987) 4950.
- [40] A. S. Clarke and H. Jonsson, *Phys. Rev. E* **47** (1993) 3975.
- [41] G. J. Dienes and G. H. Vineyard, Radiation Effects in Solids, Interscience Publishers, New York, 1957.

- [42] P. M. Derlet, D. Nguyen-Manh, and S. L. Dudarev, Phys. Rev. B **76** (2007) 054107.
- [43] J. H. Rose, J. R. Smith, and J. Ferrante, Phys. Rev. B **28** (1983) 1835.
- [44] N. W. Ashcroft and N. D. Mermin, Solid State Physics, Holt, New York, 1976.
- [45] C. J. Smithells and E. A. Brandes, Metals Reference Book, Butterworths, London, 1976.
- [46] R. W. Balluffi, J. Nucl. Mater. **69/70** (1978) 240.
- [47] G. Simmons and H. Wang, Single Crystal Elastic Constants and Calculated Aggregate Properties: a Handbook, M.I.T. Press, Cambridge, MA, 1971.
- [48] K. P. Huber and G. Herzberg, Constants of Diatomic Molecules, Van Nostrand Reinhold, New York, 1979.
- [49] Y. Mishin, M. J. Mehl, D. A. Papaconstantopoulos, A. F. Voter, and J. D. Kress, Phys. Rev. B **63** (2001) 224106.
- [50] D. E. Gray, American Institute of Physics Handbook, McGraw-Hill, New York, 1957.
- [51] C. Kittel, Introduction to Solid State Physics, Wiley, New York, 1971.
- [52] K. Maier, M. Peo, B. Saile, H. E. Schaefer, and A. Seeger, Phil. Mag. A **40** (1979) 701.
- [53] M. Tietze, S. Takaki, I. A. Schwirtlich, and H. Schultz in Point Defects and Defect Interactions in Metals: Proceedings of the Yamada Conference V, North-Holland, 1982, p. 265.
- [54] D. Nguyen-Manh, A. P. Horsfield, and S. L. Dudarev, Phys. Rev. B **73** (2006) 20101.
- [55] K. T. Kuwata, R. I. Erickson, and J. R. Doyle, Nucl. Inst. Meth. B **201** (2003) 566.